Performance of the PRAXyS X-ray Polarimeter

W.B. Iwakiri[a,*], J.K. Black[b,c], R. Cole[b], T. Enoto[d,e], A. Hayato[a], J.E. Hill[b], K. Jahoda[b], P. Kaaret[g], T. Kitaguchi[f], M. Kubota[h,a], H. Marlowe[g], R. McCurdy[g], Y. Takeuchi[h,a], T. Tamagawa[a,h]

[a] *RIKEN Nishina Center, 2-1 Hirosawa, Wako, Saitama 351-0198, Japan*
[b] *NASA Goddard Space Flight Center, Greenbelt, MD 20771, USA*
[c] *Rock Creek Scientific, 1400 East-West Hwy, Silver Spring, MD, 20910, USA*
[d] *The Hakubi Center for Advanced Research, Kyoto University, Kyoto 606-8302, Japan*
[e] *Department of Astronomy, Kyoto University, Kitashirakawa-Oiwake-cho, Sakyo-ku, Kyoto 606-8502, Japan*
[f] *Department of Physical Science, Hiroshima University, 1-3-1 Kagamiyama, Higashi-Hiroshima, Hiroshima 739-8526, Japan*
[g] *University of Iowa, Iowa City, IA, 52242, USA*
[h] *Department of Physics, Tokyo University of Science, 3-1 Kagurazaka, Shinjuku-ku, Tokyo 162-8601, Japan*

arXiv:1610.06677v1 [astro-ph.IM] 21 Oct 2016

Abstract

The performance of the Time Projection Chamber (TPC) polarimeter for the Polarimeter for Relativistic Astrophysical X-ray Sources (PRAXyS) Small Explorer was evaluated using polarized and unpolarized X-ray sources. The PRAXyS mission will enable exploration of the universe through X-ray polarimetry in the 2–10 keV energy band. We carried out performance tests of the polarimeter at the Brookhaven National Laboratory, National Synchrotron Light Source (BNL-NSLS) and at NASA's Goddard Space Flight Center. The polarimeter was tested with linearly polarized, monochromatic X-rays at 11 different energies between 2.5 and 8.0 keV. At maximum sensitivity, the measured modulation factors at 2.7, 4.5 and 8.0 keV are 27%, 43% and 59%, respectively and the measured angle of polarization is consistent with the expected value at all energies. Measurements with a broadband, unpolarized X-ray source placed a limit of less than 1% on false polarization in the PRAXyS polarimeter.

Keywords: X-ray polarimeter, PRAXyS, micropattern gas detector

1. Introduction

Cosmic X-ray polarimetry is a powerful technique for studying the physics of extreme environments such as strong gravitational fields and magnetic fields in the universe. For example, it will be possible to observe vacuum polarization effects in the extreme magnetic fields of magnetized neutron stars, where the fields are 10^{12} G or greater [1, 2]. However, X-ray polarization measurements below 10 keV have only succeeded for the Crab Nebula with measurements made by a Bragg scattering polarimeter on a sounding rocket and on the *OSO-8* satellite in the 1970s [3, 4]. In the interim, photoelectric polarimeters with greater sensitivity have been developed, first using CCDs [5, 6] and more recently gas detectors [7, 8].

To maximize sensitivity we have developed a gas polarimeter that employs the Time Projection Chamber (TPC) technique [8, 9, 10, 11, 12]. In this case the detection plane is parallel to the incident X-rays. This design allows the detector depth (and efficiency) to be increased without also increasing diffusion (limiting sensitivity). This advantage comes at the expense of true imaging of the sky. However, black holes and neutron stars have angular scales well below micro-arcsecond and sky imaging is of limited scientific utility.

The Polarimeter for Relativistic Astrophysical X-ray Sources (PRAXyS), based on this TPC polarimeter, has been selected for Phase A study as one of three Small Explorer (SMEX) missions. PRAXyS is designed to make highly sensitive measurements of the linear X-ray polarization of astronomical sources in the 2–10 keV energy band. The primary observational goals of PRAXyS are to observe a sample of black holes and neutron stars brighter than 2×10^{-11} ergs s^{-1} cm^{-2} in the 2–10 keV band, with a sensitivity to polarization fractions as small as 1%. This paper reports the polarization sensitivity of the TPC polarimeter and upper limits to the systematic errors.

Photoelectric polarimeters exploit the intrinsic polarization sensitivity of photoelectric absorption. The photoelectron produced by the interaction of an X-ray with a gas atom creates an ionization track. The initial direction of the ionization track contains information about the X-ray polarization. Gas detectors use an electric field to drift the ionization track to a multiplication and detection region. Costa et al. [7] first proposed a design in which the drift field is parallel to the X-ray direction of incidence. For this concept, maximizing sensitivity requires balancing the greater detection efficiency afforded by deeper detec-

*Corresponding author. Tel:+81-48-462-4874; FAX:+81-48-462-4640

Email address: wataru.iwakiri@riken.jp (W.B. Iwakiri)

tors with the degraded sensitivity caused by the increased diffusion as tracks drift greater distances. The TPC polarimeter breaks this competition by drifting the track perpendicular to the incident direction. This allows greater efficiency albeit at the cost of using two different detector properties to create a two dimensional image of the track [8].

PRAXyS employs a TPC polarimeter in which the charge detection plane consists of a Gas Electron Multiplier (GEM) designed by RIKEN [13] mounted over strip anodes parallel to the incident X-rays. Two-dimensional images of photoelectron tracks are created using a one-dimensional strip readout and by timing the arrival of charge [8]. The readout and detector plane is described by Hill et al. 2014 [11]. An estimate of the initial track direction is obtained from each event image.

Combining the quantum mechanical expectations for K-shell absorption and instrumental imperfections, one expects a measured distribution of photoelectron emission angles:

$$N(\phi) = A + B\cos^2(\phi - \phi_0), \tag{1}$$

where ϕ represents the azimuthal angle of the photoelectron track, ϕ_0 is the source polarization angle, and the constants A and B are characteristics of the detector and are typically dependent on energy [7, 14]. A histogram of reconstructed emission angles is called a "modulation curve". The amplitude of a modulation curve a is defined as,

$$a = \frac{f_{\max} - f_{\min}}{f_{\max} + f_{\min}} = \frac{B}{2A + B}, \tag{2}$$

where $f_{\max}$ and $f_{\min}$ are the maximum and minimum value of the modulation curve. The analyzing power of a polarimeter, called the modulation factor, μ, is the amplitude for 100% polarized input. The polarization fraction, a_p, of a source is then given by $a_p = a/\mu$.

To measure the polarization of astrophysical sources we must know the polarimeter's response to both 100% polarized and unpolarized X-rays across the energy band. We present experimental results for nearly 100% polarized X-rays in section 3.4 and unpolarized X-rays in section 3.5.

The smallest polarization which would not be observed by chance, with 99% confidence, is inversely proportional to μ and inversely proportional to the square root of the number of photons. This Minimum Detectable Polarization (MDP) is given by:

$$\mathrm{MDP} = \frac{4.29}{\mu\sqrt{F_s A_{\mathrm{eff}} \epsilon T}} \sqrt{1 + \frac{R_b}{F_s A_{\mathrm{eff}} \epsilon}}, \tag{3}$$

where F_s is the source flux, A_{eff} the mirror effective area, ϵ the polarimeter quantum efficiency, R_b the background count rate, and T is the observation time. The coefficient, 4.29 corresponds to 99% confidence that the signal is not created by chance [15]. In terms of detector parameters, the MDP scales as $1/\mu\sqrt{\epsilon}$ assuming the background count rate is negligible. The figure-of-merit for the polarimeter, which minimizes the MDP, is then $\mu\sqrt{\epsilon}$, where ϵ includes losses due to, for example, an X-ray window and events rejected in analysis. To achieve a statistical precision estimated by the MDP formula, systematic errors must be lower than the MDP.

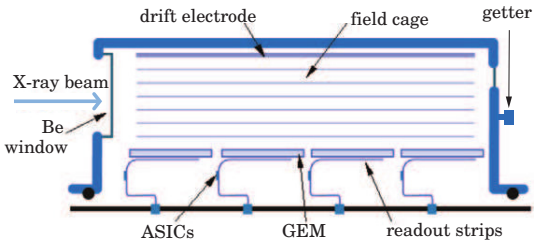

Figure 1: Cross-section of the PRAXyS flight polarimeter.

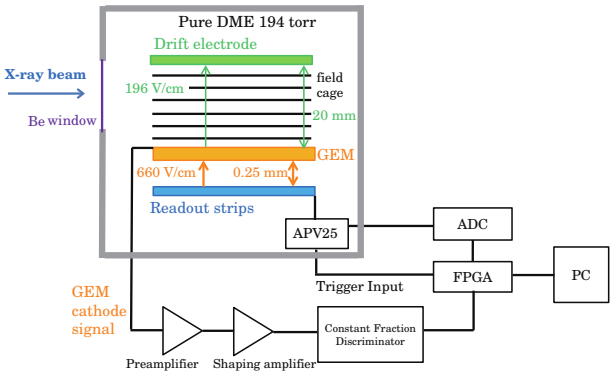

Figure 2: Test setup for performance tests of the prototype polarimeter module for PRAXyS using the unpolarized X-ray source and the linear polarized X-ray beam. The electronics inside the gas volume employs the flight design. GSE electronics are employed outside.

2. Experimental Setup

We measured the polarization sensitivity of the PRAXyS polarimeter using a single detector module of the flight design. The energy dependent sensitivity to $\sim$ 100% polarized X-rays over the full range of detector interaction positions was measured at the X-19A beamline at Brookhaven National Laboratory, National Synchrotron Light Source (BNL-NSLS) facility in September 2014. To search for systematic errors that would create a false modulation, we measured the response to a broadband, unpolarized source with a bremsstrahlung spectrum, at the NASA Goddard Space Flight Center (NASA/GSFC).

2.1. Overview of the PRAXyS Polarimeter

The PRAXyS polarimeter employs a segmented approach, with four identical readouts arranged in series, parallel to the X-ray beam, as illustrated in Fig. 1. The four readouts share a common gas volume as well as a common set of field shaping electrodes [10]. The measurements presented in this paper are made with a single read-

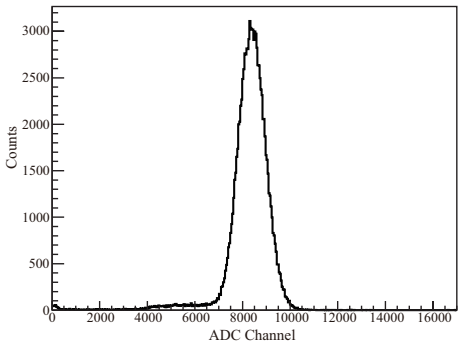

Figure 3: Typical ADC spectrum of 6.4 keV X-rays. The energy resolution (FWHM) is about 16% at 6.4 keV.

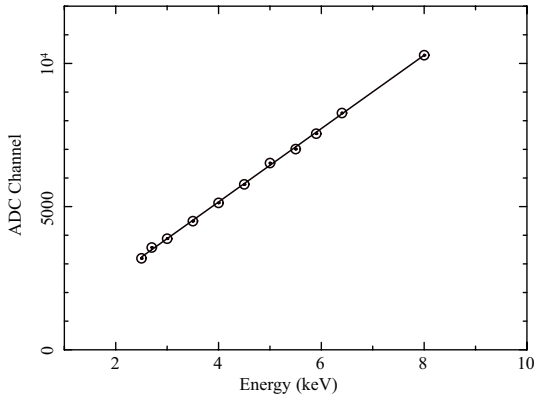

Figure 4: The calibration curve of the ADC channel versus input energy obtained at BNL-NSLS X-19A beam line. The error in each data set is less than 0.5%. The black line is the best-fit linear model; ADC = 36 + 1281 × E (keV).

out, identical to the flight design, and a flight-equivalent set of field shaping electrodes, sized for a single readout.

A block diagram of the test set-up is shown in Fig. 2. The active volume for incident X-rays is 78(l) × 30(w) × 20(h) mm^3 between the GEM and the drift electrode. However, the maximum drift distance for these experiments is defined by the size of the beryllium entrance window, which is 14 mm. The polarimeter was filled with dimethyl ether (DME) to a pressure of 193.5 Torr at a temperature of 299.4 K. The pitch of the readout strips (121 μm) and the drift velocity multiplied by the sampling time (50 ns) defines the dimensions of the image pixels. Magboltz[1] was used to estimate the drift field required to obtain a drift velocity for a two dimensional image with square pixels (A drift velocity of 0.242 cm μs^{-1} requires an applied drift field of 196 V cm^{-1}). The drift velocity calculation was confirmed by measurement. A transfer field of 660 V cm^{-1} was applied across the 0.25 mm transfer gap between the GEM and the readout strips. This value is a compromise between efficient charge collection and asymmetric diffusion in the transfer gap. Figure 3 shows the typical energy spectrum obtained at 6.4 keV, with full-width-at-half-maximum (FWHM) energy resolution of 16%. As in the flight design, the signals from the strip electrodes were read out via an APV25 Application Specific Integrated Circuit (ASIC) [16]. Signal processing outside the gas volume was performed with ground support equipment (GSE) electronics. The GEM cathode signal was amplified and shaped by an ORTEC 142AH preamplifier and an ORTEC 671 shaping amplifier and digitized by a TENNELEC TC451 constant fraction discriminator to generate a trigger signal in the Field Programmable Gate Array (FPGA) to readout out the ASIC. A more detailed description of the readout system is provided in Black et al. 2010 [9].

[1] http://consult.cern.ch/writeup/magboltz/

2.2. Beamline measurement

The response to polarized X-rays was measured at eleven different monochromatic energies from 2.5 to 8.0 keV. The X-ray beam was collimated to < 0.25 mm, and $\sim 1.5\times10^5$ counts were obtained at each energy except at 2.5 keV, where we collected $\sim 3\times10^4$ counts. Data were obtained at a range of drift heights. Figure 4 shows that the relation between pulse height and energy is quite linear. The polarimeter was inclined at approximately -45° relative to the polarization vector of the synchrotron beam.

The polarization of the synchrotron beam itself was independently measured using a scattering polarimeter which consists of a cylindrical Be scatterer and perpendicularly placed solid-state detector. The data at 7.8 and 10 keV are consistent with a beam polarization of 94% (Enoto et al. 2014 [12], Appendix A). We assume that the beam polarization is 94% at all energies.

3. Analysis and Results

3.1. Data processing

An image of each photoelectron track is formed from pixels consisting of 30 strips × 30 time bins, corresponding to 3.63 × 3.63 mm^2. Both the offset (pedestal) value for each strip electrode and the common mode noise (median pulse height response of each strip not contained in the event) is subtracted prior to constructing the image. Only pixels that contain charge greater than 3 times the root mean square (RMS) noise are included in the image analysis. The APV25 ASIC applies a 50 ns shaping time to each signal. The response is de-convolved with the measured ASIC response $h(t)$ to an internal test pulse. If the input $f(t)$ and output signal $o(t)$ of a time series relate to $h(t)$ according to:

$$o(t) = \int h(t-t')f(t')dt'. \quad (4)$$

And the Fourier transformations O, H and F in the Fourier space T are:

$$O(T) = H(T)\cdot F(T). \quad (5)$$

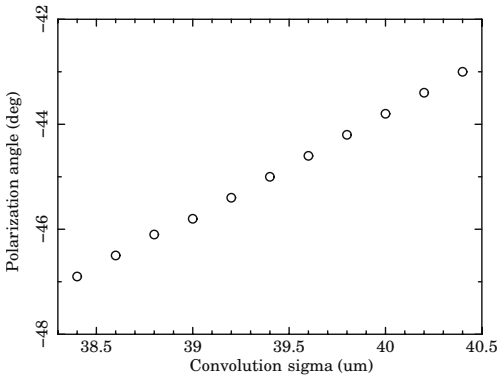

Figure 5: Polarization angle of a 2.7 keV polarized X-ray beam as a function of the width of the Gaussian convolution along the time axis.

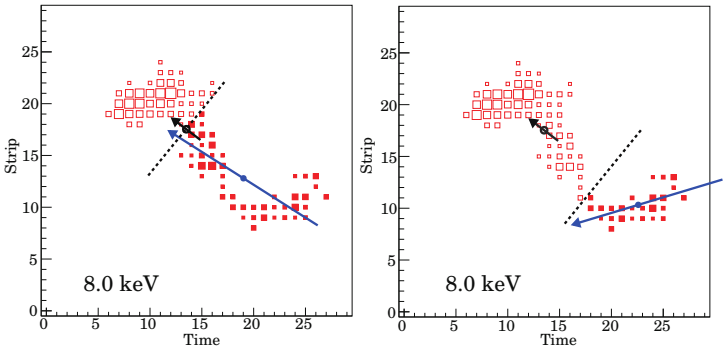

Figure 6: Previous track reconstruction algorithms [8] (left panel) use the initial half of the track. The track is separated along the minor axis of the charge distribution (dashed line) that is perpendicular to the major axis (black arrow) and passed through the centroid of the charge distribution (black dot). We employ a new method that iteratively cuts the charge distribution until a variance/skewness test that identifies straight track segments is satisfied. Only the filled pixels in the right panel are used in the final estimate. For this track, the estimated direction shifts by ∼50 degrees between the standard two stage reconstruction and our improved method.

The original input signal is derived as the inverse-Fourier transformation product of $O(T)/H(T)$ (deconvolution of electronics response).

The required transfer field for efficient charge collection results in an asymmetry in the intrinsic transverse and longitudinal diffusion. The sampling of the diffusion further increases the asymmetry, as the transverse diffusion is a significant fraction of a pixel (defined by readout strip pitch) while the longitudinal diffusion is a negligible fraction of a pixel (defined by drift velocity in the transfer gap multiplied by the sampling time). The asymmetric diffusion effects are accounted for by applying a Gaussian convolution in the time axis.

We multiply the Fourier transformation G of the Gaussian $g(t)$ in the Fourier space,

$$\hat{F}(T) = O(T) \cdot G(T)/H(T). \quad (6)$$

Thus, the corrected input signals using a Gaussian convolution $g(t)$ is the inverse-Fourier transformation of $\hat{F}(T)$.

The standard deviation, σ_t, of the Gaussian convolution was calibrated at the BNL-NSLS beamline using polarized 2.7 keV X-rays. The resulting polarization angle as a function of convolution sigma is shown in Fig. 5. We performed an iterative process to determine the correct σ_t. Since the polarimeter was inclined at approximately $-45°$ relative to the polarization vector of the beam, we initially used a best-fit Gaussian width of 39.4 μm which corresponds to an angle of $-45°$. This resulted in an average angle of -46.0 over the energy range. We iterated the process, this time using a best-fit Gaussian width of 38.9 μm which equalized the polarization angle to $-46.1°$.

3.2. Angular reconstruction

Previous analysis has used a two-stage moments analysis to estimate photoelectron directions for individual events [8]. In the first stage, the principal axes are estimated using the second order central moments of the charge distribution from the entire track. The previous method is illustrated in the left panel of Fig. 6, where the size of each symbol is proportional to the recorded charge, and each symbol corresponds to a single 121 μm resolution element. The black arrow Fig. 6 (left) shows the direction of the major axis; the dot represents the centroid of the charge distribution. For tracks with high eccentricity, the track is divided along the minor axis (dashed line) and the half with higher charge density (the Bragg peak, which represents the end of the track) is ignored. The photoelectron direction is then estimated from moments fit to the first half of the track (blue arrow). However, for long and curved tracks as in Fig. 6, the two-stage estimate may still be inaccurate. We have developed a new image reconstruction method [17] summarized here.

First, the second moment (variance) and the third moment (skewness) along the major and minor principal axes are used to judge whether or not a track is curved. For curved tracks, the charge distribution is repeatedly cut off in 0.5 pixel steps along the major axis of the entire charge distribution until the variance and skewness of the remaining portion of the image are below set thresholds (Fig. 6 right). Lastly, the initial angle of the photoelectron track is reconstructed from the central moments method using the initial part of the track that satisfied the variance/skewness conditions. The blue arrow in the right panel of Fig. 6 shows the result obtained by the new method, which is noticeably more accurate than the two-stage reconstruction in the left panel. The improved estimate of the track direction leads to higher values of μ.

3.3. Event selection

In principle, the reconstructed photoelectron emission angle gives the polarization state of every X-ray. However, instrumental effects can obscure the emission direction, es-

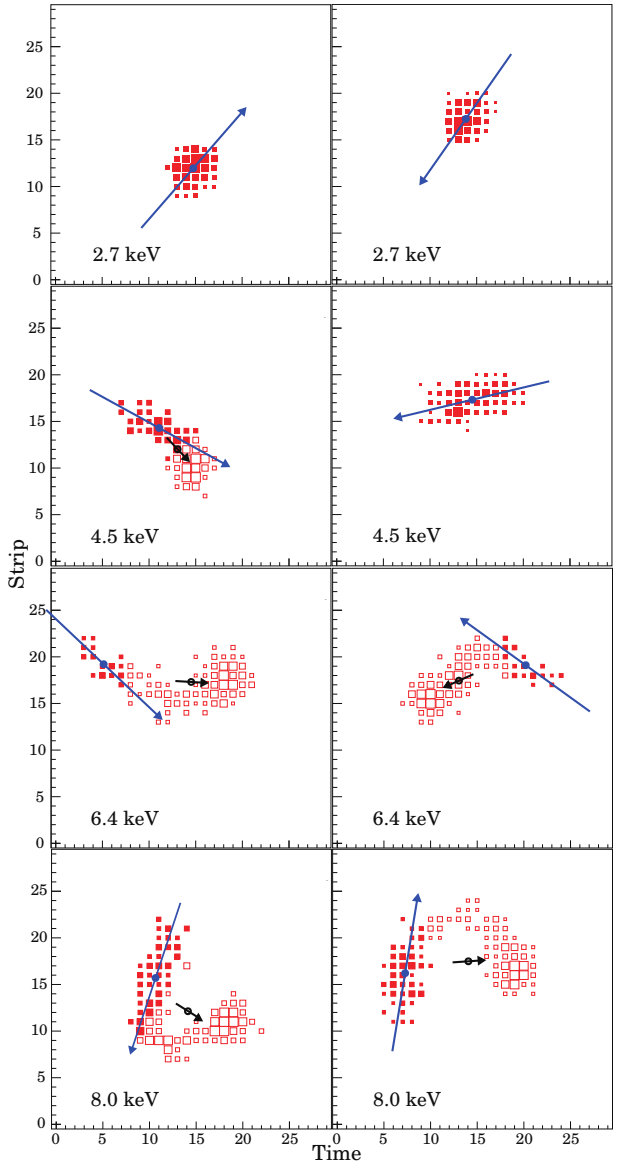

Figure 7: Same as the right panel of the Fig.6 but for four energies.

pecially at lower energies, eliminating the polarization information for some X-rays. These events essentially form an unpolarized background. The obscuring effects include Coulomb scattering, electron diffusion, charge associated with an isotropically emitted Auger electron and foreshortening of tracks when projected onto the readout plane. These instrumental effects are confirmed by Monte-Carlo simulation [18] and are characterized by low eccentricity.

To minimize the MDP, we maximize $\mu\sqrt{\epsilon}$, which is the figure of merit explained in Section 2, by excluding events with eccentricity below an experimentally determined and pulse height dependent threshold. The event threshold, $e_{\rm th}$, for the measured pulse height, PH, is given by:

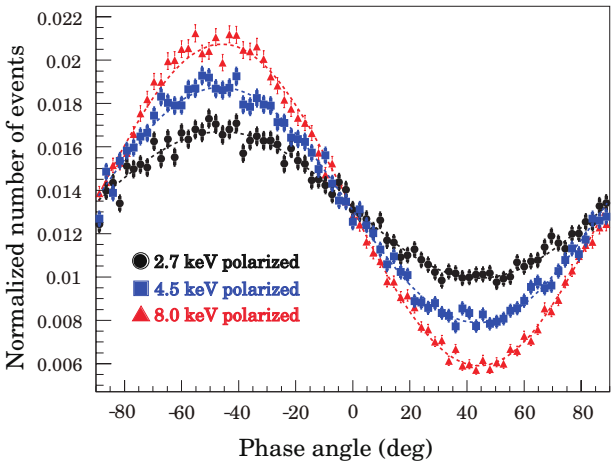

Figure 8: Modulation curves for three energies at an average drift height of 8 mm(averaged from 6 mm, 8 mm and 10 mm). The effective modulation factors μ of 2.7 keV polarized (black), 4.5 keV polarized (blue) and 8.0 keV polarized (red) are 26.92±0.66%, 43.38±0.59% and 59.14±0.55%, respectively.

$$e_{\rm th} = \begin{cases} 0.48 & (\text{PH}<5\ \text{keV}) \\ -1.1604+0.4882\cdot E-0.0321\cdot E^2 & (5\ \text{keV}\leq\text{PH}\leq 8\ \text{keV}) \\ 0.69 & (\text{PH}>8\ \text{keV}). \end{cases} \quad (7)$$

The fractional increase in μ is larger than the fractional decrease in $\sqrt{\epsilon}$, thus improving the overall figure-of-merit $\mu\sqrt{\epsilon}$. Similar measurements for an alternate detector geometry [19, 20] also demonstrate the benefit of an eccentricity based selection.

3.4. Performance tests with polarized X-rays at BNL-NSLS

Examples of track images taken at the BNL-NSLS, after the data processing described in the previous section, are shown in Fig. 7. Figure 8 shows histograms of emission angles for three different polarized X-ray energies. The fitting results show that the measured effective modulation factors, μ, are 26.92%, 43.38% and 59.14% at 2.7, 4.5 and 8.0 keV, respectively. We show the summary of μ and polarization angle as a function of energy in Fig. 9 and Table 1. The signal acceptance after eccentricity cuts is also shown in Table 1. The measured values of μ versus E are quite similar to those of Li et al. 2015 [19]. This is not surprising as our geometry and Li et al. have similar products of pressure and pixel size, so that track lengths, measured in pixels, is similar. Figure 9 (right) shows that the reconstructed polarization angle is independent of energy. The mean polarization angle ϕ is $-46.1^\circ \pm 0.1^\circ$, it is consistent with the expected angle within statistical error.

3.5. Performance tests with unpolarized X-ray

With modulation similar to a pixel polarimeter, the greater quantum efficiency of the TPC polarimeter will allow it to achieve higher sensitivity only if systematic errors

Table 1: Best-fit parameters for the modulation curves. All errors denote 90% error level.

Energy (keV)	μ (%)	ϕ_0 (degree)	f^*	χ^2/d.o.f†
2.5	24.53 ± 2.10	-45.10 ± 2.67	0.76	19.70/17
2.7	26.92 ± 0.66	-45.90 ± 0.76	0.76	94.85/97
3.0	32.61 ± 0.65	-47.26 ± 0.62	0.79	105.65/97
3.5	36.63 ± 0.61	-45.82 ± 0.53	0.85	89.78/97
4.0	40.90 ± 0.60	-45.85 ± 0.46	0.91	125.45/97
4.5	43.38 ± 0.59	-46.35 ± 0.43	0.92	132.08/97
5.0	46.00 ± 0.58	-46.47 ± 0.40	0.91	142.29/97
5.5	49.24 ± 0.58	-45.88 ± 0.38	0.90	122.61/97
5.9	52.48 ± 0.57	-46.09 ± 0.35	0.91	141.10/97
6.4	54.42 ± 0.57	-46.44 ± 0.34	0.89	127.62/97
8.0	59.14 ± 0.55	-45.77 ± 0.31	0.87	112.24/97

$*$: the signal acceptance after eccentricity cuts.
$\dagger$: degrees of freedom.

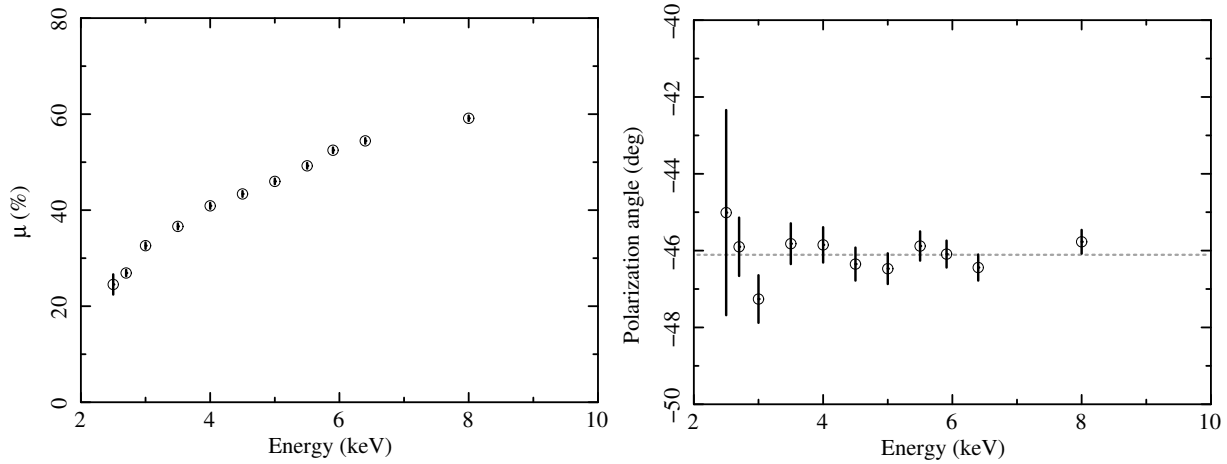

Figure 9: (Left) Modulation factor as a function of an incident X-ray energy. (Right) Same as left panel but for polarization angle. Dotted line shows the mean polarization angle.

that create false modulation are small compared to the statistical limits. PRAXyS employs multiple strategies, including instrument rotation, to eliminate such errors.

We collected 2.6 million events from an unpolarized broadband Bremsstrahlung spectrum that peaks around 3 keV with a 5 keV endpoint shown in the left panel of Fig. 10. For the PRAXyS mission design, the worst case pointing error (including alignment terms) is 1 arcmin, which corresponds to 1.3 mm at the center of the detector. Therefore, to simulate the rotation, we took 36 measurements, each with 64,000 events which went around the compass in 10 degree steps. The mean drift distance, d, from the interaction point to the GEM, is $d = 8 + 1.3 \sin\theta$ (mm). An 8 mm drift height corresponds to the optical axis of the detector. If the detector were rotating about a different axis, the apparent mean drift distance would vary as above. We simulate this rotation by moving a collimated pencil beam in a circle on the detector aperture. Theta is also the amount by which each data set must be shifted to transform detector coordinates to laboratory (or sky) coordinates. We co-added the data in effective sky coordinates using θ as the ephemeris.

We reconstructed the data following the analysis steps described in section 3.1, 3.2 and 3.3. After the eccentricity cut based on pulse height, 2.1 million events remained. The measured modulation factor is 0.10% ± 0.16% (90% confidence level) shown in Fig. 10 (right). The MDP associated with these data, using an average value of μ weighted by the counts spectrum in Fig. 10 (left) is 0.87%. Thus the polarimeter is capable of making statistics limited polarization detections at levels below 1%. For true polarization fractions of 2% (5%), the polarimeter will make 4.6 σ (11.6 σ) detections from similar datasets (2.1×10^6 counts after eccentricity selection).

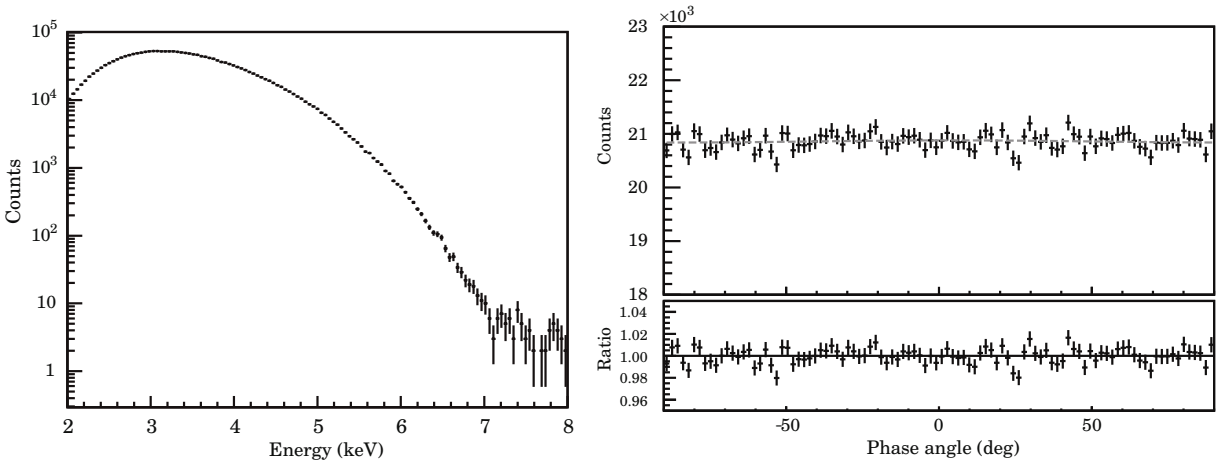

Figure 10: Spectrum (left) and modulation curve (right) for the unpolarized broadband Bremsstrahlung source. The modulation factor $\mu = 0.10 \pm 0.16\%$ with χ^2 / d.o.f = 113.52 / 97.

4. Conclusion

We evaluated the performance of the prototype polarimeter for PRAXyS using the linearly-polarized X-ray source at BNL-NSLS between 2.5 and 8.0 keV. With unpolarized X-rays, we measured an upper limit to the expected systematic errors that would lead to false polarization. These measurements demonstrate that the polarimeter meets or exceeds the sensitivity required for PRAXyS to reach its scientific goals. The results are summarized below:

- After the image reconstruction of photoelectron track and the optimized eccentricity cut, the modulation factors, μ, of the PRAXyS polarimeter are 27%, 43% and 59% at 2.7, 4.5 and 8.0 keV, respectively.
- Measured polarization angles are constant relative to incident energy. For small polarization fractions, the error on the polarization angle will be limited by statistics. For large polarization fractions and significant measurements, the maximum error will be less than 1°. These values exceed the requirements levied on the PRAXyS polarimeters.
- False modulation is not detected in a continuum dominated spectrum, representative of that expected from astronomical observations, with over 2 million counts, which is comparable to the number of photons needed to detect a 1% polarization.

Acknowledgments

This work was partially supported via proposal 13-APRA13-0141 in response to the NASA Astrophysics Research and Analysis solicitation NNH13ZDA001N-APRA and MEXT KAKENHI Grant Number 24105007. The authors would like to acknowledge the support of Syed Khalid at the X19A beamline at the BNL-NSLS. W.B. Iwakiri was supported by JSPS KAKENHI, Grant-in-Aid for JSPS Fellows, 25-5312. We also thank the two anonymous referees whose comments have helped us improve the presentation of these results.

References

[1] P. Meszaros, W. Nagel, X-ray pulsar models. I - Angle-dependent cyclotron line formation and comptonization, ApJ 298 (1985) 147–160. doi:10.1086/163594.

[2] P. Ghosh, L. Angelini, M. Baring, W. Baumgartner, K. Black, J. Dotson, A. Harding, J. Hill, K. Jahoda, P. Kaaret, T. Kallman, H. Krawczynski, J. Krolik, D. Lai, C. Markwardt, H. Marshall, J. Martoff, R. Morris, T. Okajima, R. Petre, J. Poutanen, S. Reynolds, J. Scargle, J. Schnittman, P. Serlemitsos, Y. Soong, T. Strohmayer, J. Swank, Y. Tawara, T. Tamagawa, White Paper on GEMS Study of Polarized X-rays from Neutron Stars, ArXiv e-printsarXiv:1301.5514.

[3] R. Novick, M. C. Weisskopf, R. Berthelsdorf, R. Linke, R. S. Wolff, Detection of X-Ray Polarization of the Crab Nebula, ApJL 174 (1972) L1. doi:10.1086/180938.

[4] M. C. Weisskopf, E. H. Silver, H. L. Kestenbaum, K. S. Long, R. Novick, A precision measurement of the X-ray polarization of the Crab Nebula without pulsar contamination, ApJL 220 (1978) L117–L121. doi:10.1086/182648.

[5] H. Tsunemi, K. Hayashida, K. Tamura, S. Nomoto, M. Wada, A. Hirano, E. Miyata, Detection of X-ray polarization with a charge coupled device, Nuclear Instruments and Methods in Physics Research A 321 (1992) 629–631. doi:10.1016/0168-9002(92)90075-F.

[6] G. Buschhorn, R. Kotthaus, W. Kufner, W. Rössl, M. Rzepka, K. H. Schmidt, H. Genz, H.-D. Gräf, P. Hoffmann-Stascheck, U. Nething, A. Richter, W.-R. Dix, G. Illing, M. Lohmann, J. Pflüger, B. Reime, L. Schildwächter, X-ray polarimetry using the photoeffect in a CCD detector, Nuclear Instruments and Methods in Physics Research A 346 (1994) 578–588. doi:10.1016/0168-9002(94)90595-9.

[7] E. Costa, P. Soffitta, R. Bellazzini, A. Brez, N. Lumb, G. Spandre, An efficient photoelectric X-ray polarimeter for the study of black holes and neutron stars, Nature 411 (2001) 662–665. arXiv:astro-ph/0107486.

[8] J. K. Black, R. G. Baker, P. Deines-Jones, J. E. Hill, K. Jahoda, X-ray polarimetry with a micropattern TPC, Nuclear Instru-

ments and Methods in Physics Research A 581 (2007) 755–760. doi:10.1016/j.nima.2007.08.144.

[9] J. K. Black, P. Deines-Jones, J. E. Hill, T. Iwahashi, K. Jahoda, P. Kaaret, T. R. Kallman, C. J. Martoff, Z. Prieskorn, J. Swank, T. Tamagawa, The GEMS photoelectric x-ray polarimeters, in: Society of Photo-Optical Instrumentation Engineers (SPIE) Conference Series, Vol. 7732 of Society of Photo-Optical Instrumentation Engineers (SPIE) Conference Series, 2010, p. 0. doi:10.1117/12.857736.

[10] J. E. Hill, R. G. Baker, J. K. Black, M. J. Browne, W. H. Baumgartner, E. M. Caldwell, J. D. Cantwell, A. Davies, A. B. Desai, P. L. Dickens, N. K. Dobson, R. L. Foxwell, A. S. Francomacaro, D. Gall, K. J. Gregory, S. Griffiths, A. Hayato, R. O. Hampshire, T. Hwang, M. D. Jhabvala, K. Jahoda, P. Kaaret, S. J. Lehtonen, N. F. Martin, J. S. Mohammed, K. Montt de Garcia, A. Morell, D. S. Nolan, R. E. Russell, M. A. Sampson, J. A. Sanders, K. Simms, M. J. Singer, J. H. Swank, T. Tamagawa, A. Weaver, S. N. Yerushalmi, J. J. Xu, The design and qualification of the GEMS x-ray polarimeters, in: Society of Photo-Optical Instrumentation Engineers (SPIE) Conference Series, Vol. 8443 of Society of Photo-Optical Instrumentation Engineers (SPIE) Conference Series, 2012, p. 1. doi:10.1117/12.928435.

[11] J. E. Hill, J. K. Black, T. J. Emmett, T. Enoto, K. M. Jahoda, P. Kaaret, D. S. Nolan, T. Tamagawa, Design improvements and x-ray performance of a time projection chamber polarimeter for persistent astronomical sources, in: Society of Photo-Optical Instrumentation Engineers (SPIE) Conference Series, Vol. 9144 of Society of Photo-Optical Instrumentation Engineers (SPIE) Conference Series, 2014, p. 1. doi:10.1117/12.2057259.

[12] T. Enoto, J. K. Black, T. Kitaguchi, A. Hayato, J. E. Hill, K. Jahoda, T. Tamagawa, K. Kaneko, Y. Takeuchi, A. Yoshikawa, H. Marlowe, S. Griffiths, P. E. Kaaret, D. Kenward, S. Khalid, Performance verification of the Gravity and Extreme Magnetism Small explorer (GEMS) x-ray polarimeter, in: Society of Photo-Optical Instrumentation Engineers (SPIE) Conference Series, Vol. 9144 of Society of Photo-Optical Instrumentation Engineers (SPIE) Conference Series, 2014, p. 4. doi:10.1117/12.2056841.

[13] T. Tamagawa, A. Hayato, F. Asami, K. Abe, S. Iwamoto, S. Nakamura, A. Harayama, T. Iwahashi, S. Konami, H. Hamagaki, Y. L. Yamaguchi, H. Tawara, K. Makishima, Development of thick-foil and fine-pitch GEMs with a laser etching technique, Nuclear Instruments and Methods in Physics Research A 608 (2009) 390–396. arXiv:0910.0406, doi:10.1016/j.nima.2009.07.014.

[14] T. E. Strohmayer, T. R. Kallman, On the Statistical Analysis of X-Ray Polarization Measurements, ApJ 773 (2013) 103. arXiv:1306.3885, doi:10.1088/0004-637X/773/2/103.

[15] M. C. Weisskopf, R. F. Elsner, V. M. Kaspi, S. L. O'Dell, G. G. Pavlov, B. D. Ramsey, X-Ray Polarimetry and Its Potential Use for Understanding Neutron Stars, in: W. Becker (Ed.), Astrophysics and Space Science Library, Vol. 357 of Astrophysics and Space Science Library, 2009, p. 589. doi:10.1007/978-3-540-76965-1_22.

[16] M. J. French, L. L. Jones, Q. Morrissey, A. Neviani, R. Turchetta, J. Fulcher, G. Hall, E. Noah, M. Raymond, G. Cervelli, P. Moreira, G. Marseguerra, Design and results from the APV25, a deep sub-micron CMOS front-end chip for the CMS tracker, Nuclear Instruments and Methods in Physics Research A 466 (2001) 359–365. doi:10.1016/S0168-9002(01)00589-7.

[17] T. Kitaguchi, in preparation.

[18] T. Kitaguchi, T. Tamagawa, A. Hayato, T. Enoto, A. Yoshikawa, K. Kaneko, Y. Takeuchi, K. Black, J. Hill, K. Jahoda, J. Krizmanic, S. Sturner, S. Griffiths, P. Kaaret, H. Marlowe, Monte-Carlo estimation of the inflight performance of the GEMS satellite x-ray polarimeter, in: Space Telescopes and Instrumentation 2014: Ultraviolet to Gamma Ray, Vol. 9144 of Society of Photo-Optical Instrumentation Engineers (SPIE) Conference Series, 2014, p. 91444L. doi:10.1117/12.2057334.

[19] H. Li, H. Feng, F. Muleri, R. Bellazzini, M. Minuti, P. Soffitta, A. Brez, G. Spandre, M. Pinchera, C. Sgró, L. Baldini, R. She, E. Costa, Assembly and test of the gas pixel detector for X-ray polarimetry, Nuclear Instruments and Methods in Physics Research A 804 (2015) 155–162. arXiv:1509.05595, doi:10.1016/j.nima.2015.09.060.

[20] M. C. Weisskopf, B. Ramsey, S. ODell, A. Tennant, R. Elsner, P. Soffitta, R. Bellazzini, E. Costa, J. Kolodziejczak, V. Kaspi, F. Mulieri, H. Marshall, G. Matt, R. R., The Imaging X-ray Polarimetry Explorer (IXPE), in: Space Telescopes and Instrumentation 2016: Ultraviolet to Gamma Ray, Vol. 9905 of Society of Photo-Optical Instrumentation Engineers (SPIE) Conference Series, 2016. doi:10.1117/12.2235240.